Probing topological phase transitions in the Aubry-Andre-Harper model via high-harmonic generation

Nivash R ,[*] Jayendra N. Bandyopadhyay , and Amol R. Holkundkar

Department of Physics, Birla Institute of Technology and Science - Pilani, Rajasthan 333031, India

We study the high-harmonic generation (HHG) in the Aubry-Andre-Harper (AAH) model. The modulating phase of the AAH model is used as a control parameter while preserving the chiral symmetry hosting the zero-energy edge states. The harmonic yield in a particular energy range exhibits a strong dependence on the control parameter with a clear separation of the region of topologically trivial and nontrivial phases of the system. The threshold for the harmonic yield is found to serve as an all-optical tool for detecting topological phases. We extended our study with broken chiral symmetry by including the onsite potential. The introduction of the onsite potential lifts the degeneracy in the edge states, which affects the harmonic enhancement. Furthermore, it is also observed that the system's onsite strength can control the HHG yield.

I. INTRODUCTION

The high-harmonic generation (HHG) has been extensively studied in the gas phase over the last decades; it gives us a promising route to produce highly tunable extreme-ultraviolet (XUV) pulses in the attosecond regime [1], along with the opportunity to investigate the electron dynamics in atoms and molecules on their natural timescales [2,3]. With the advancement of technology, midinfrared sources are opening new avenues in the strong field interaction with the solids, as witnessed from the pioneering work of Ghimire *et al.* [4]. The HHG from solids promises a compact source of XUV radiation and attosecond spectroscopy [5–7]. Moreover, it also enabled us to explore the countless possibilities in condensed matter physics, like exploring the large-band-gap dielectrics [5], retrieving the band structure [8], the effect of vacancy defects [9], the petahertz current in solids [5], HHG in graphene [10,11] and transition metal dichalcogenides [12], Bloch oscillations in solids [13,14], and many more.

The invention of the quantum Hall effect [15] escalated the research directions toward exploring the topological phases of matter. The topological material exhibits the insulating property in the bulk but has a conducting edge state, unaffected by the perturbations and defects. It enabled the researchers to explore the strong field phenomenon in topological condensed matter physics, especially the high-harmonic generation.

The HHG from the topological materials or, in general, solids can be understood in terms of intraband and interband current contributions [16]. The motion of electron within a band contributes to the intraband emission with the photon energy below the band gap. However, the electron transitions from one band to the other band constitute the emission (above the band-gap energy) caused by the interband current. In the case of the topological materials, an edge state in the

band gap enhances the interband transitions, strengthening the high-harmonic emission. In the later part of this paper, we will see how the characteristics of the HHG emission by the topological material might work as a diagnostic tool to distinguish between the topological phases.

The contribution of the edge state in the HHG processes is widely studied in the context of the one-dimensional (1D) Su-Schrieffer-Heeger (SSH) model [17–19], the extended SSH model [20], the Aubry-Andre-Harper (AAH) model [21], and the Kiteav model [22,23]. Furthermore, the HHG spectrum is an all-optical probe used to extract topological information using the helicity [24,25] or circular dichroism [26] of the emitted photons in the Haldane model. With the above theoretical studies, whether the HHG spectrum shows unique characteristic features that exhibit topology remains to be seen. However, recently, an *ab initio* simulation of HHG [27] shed light on the universal behavior of topological signatures in the HHG spectra.

This paper uses a control parameter in the Aubry-Andre Harper model for the HHG processes and studies the topological phase transitions. In the past, this model was used to study the dynamics of particles in quasiperiodic systems. This AAH model can be experimentally accessible using photonic crystals [28,29] and an optical waveguide array [28,30,31]. The quasiperiodicity of the AAH model in the form of a cosine modulation has its periodicity, which determines whether modulation is incommensurate (irrational) or commensurate (rational) with lattice spacing. Moreover, quasiperiodicity may be included in the terms of onsite and hopping. The incommensurate hopping modulation leads to Anderson-type localization [32], and the commensurate hopping modulation term leads to the appearance of zero-energy edge states [33,34]. Interplay between both quasiperiodic modulations was studied in [32]. The one-dimensional quasicrystals (QC) were found to be topologically nontrivial, with the periodically modulating parameter providing an additional degree of freedom, which can be mapped into the two-dimensional

---

*Contact author: nivash1807@gmail.com

115103-1

Hofstadter model, investigated theoretically [31,35] and experimentally [28,29].

The discrete symmetries of the system classify the properties of a topological insulator (TI) [36,37]. One of them is the chiral symmetry or sublattice symmetry (in the case of 1D TIs), which is responsible for the conservation of zero-energy edge states that are reflected in the anticommutation property between the chiral operator and the bulk Hamiltonian. The role of breaking the chiral symmetry in topological insulators has been investigated using HHG mechanism [19], and the emergence of opposite chirality in Weyl semimetals has been studied recently under strong laser excitation [38,39]. Recent studies claim that HHG can be a sensitive probe for chirality in higher-dimensional systems like the tellurium crystals [40], the surface of silicon dioxide, and magnesium oxide [41] by driving circularly polarized light.

In this work, we have investigated the HHG using the AAH model with off-diagonal hopping while preserving chiral symmetry. We use the modulating phase of the AAH model as a control parameter, which reveals the characteristic signatures in the HHG yield as follows: (i) The harmonic yield has a strong dependence on the control parameter and ability to differentiate between the topological and trivial phases. The transitions from the edge states (topological nontrivial) result in the higher-harmonic yield. However, for trivial phase (no edge states) the yield is observed to be lower. (ii) The harmonic yield is suppressed due to interference of interband and intraband currents when the control parameter is around the topological phase transitions. (iii) The onsite strength (broken chiral symmetry) also plays a crucial role in determining harmonic yield. This paper is organized as follows: The theoretical aspects are presented in Sec. II, followed by the results and discussion in Sec. III, and finally the summary in Sec. IV.

II. METHODOLOGY

A. Model

We study here the 1D AAH with off-diagonal hopping [33] which is described by the following Hamiltonian of the form

$$H_0 = \sum_{n=1}^{N} \eta[c_{n+1}^\dagger c_n + \text{H.c.}],\tag{1}$$

where $c_n^\dagger$ and c_n are creation and anhilation operators, respectively. Here, η is the hopping potential and has the form $\eta = \eta_0[1 + \lambda \cos(2\pi b n + \phi)]$, with λ being the amplitude of quasiperiodicity and modulating phase factor ϕ. The quasiperiodicity can be encoded through the cosine modulation with periodicity $1/b$, where b, the modulating frequency, controls the quasiperiodicity between commensurate and incommensurate cases. Depending on the value of b (here in this work, b takes the form $b = p/q = \frac{1}{2}$ with "q" bands. The modulating parameter $\phi \in [0, 2\pi]$ appears as the additional degree of freedom (d.o.f.) [42], which affects the topological nature of the AAH model [29]. It allows us to map the two-dimensional (2D) Hofstadter model, which describes electrons hopping on a 2D square lattice in a perpendicular magnetic field with $2\pi b$ magnetic flux quanta per unit cell [31]. In this work, we have set $\eta_0 = 0.5$ a.u., $\lambda = 0.2$ a.u.,
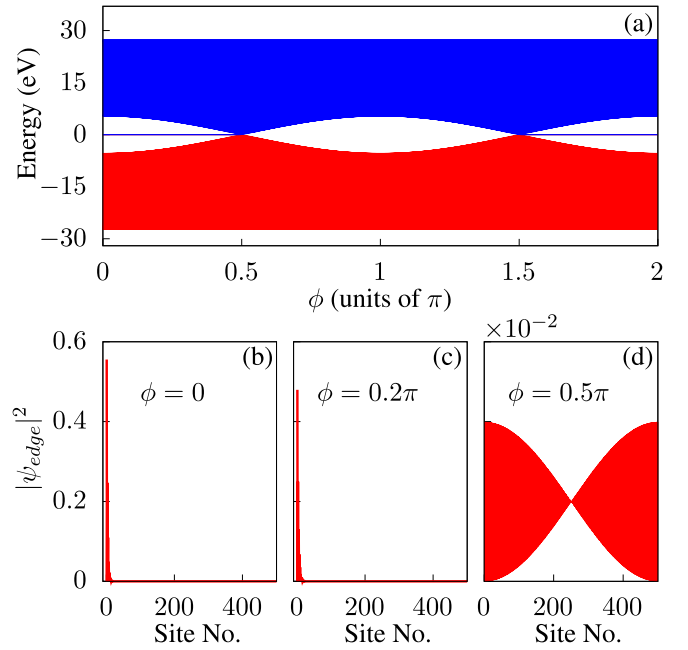

FIG. 1. The energy spectrum with 500 lattice sites as a function of ϕ (a) The red and blue colors represent the "valence band" (VB) (occupied states) and "conduction band" (CB) (unoccupied states), respectively. The lower plots show the probability distribution of the edge state in the AAH with off-diagonal hopping for three different values: $\phi = 0\pi$ (b), $\phi = 0.2\pi$ (c), and $\phi = 0.5\pi$ (d).

and $N = 500$ lattice sites. The energy eigenvalues are plotted in Fig. 1(a) with respect to ϕ, showing degenerate pairs of edge states in the regions $0 < \phi < 0.5\pi$ and $1.5\pi < \phi < 2\pi$. Further, we plot the probability of zero-energy eigenstate for specific values of $\phi = 0$, 0.2π, and 0.5π, which confirms the localization of edge states as shown in Figs. 1(b)–1(d). The states are localized at the edge for $\phi = 0$ in the probability plot, and localization strength decreases at $\phi = 0.2\pi$. It is observed that the localization strength decreases with ϕ, and the state becomes delocalized at $\phi = 0.5\pi$ and goes into the bulk part of the chain. The importance of localization and the presence of edge states will be discussed in detail in the upcoming section.

This model preserves chiral symmetry [43], i.e., $C^\dagger H_0(k) C = -H_0(k)$, where $C = \sigma_z$ is the chiral opertor. The periodicity in the modulating frequency b causes the model to dimerize [44], i.e., there will be q number of sublattices. Hence, the above equation is modified as

$$H_0 = \sum_{n=1}^{N} [\eta_1 c_{n,A}^\dagger c_{n,B} + \eta_2 c_{n,B}^\dagger c_{n+1,A} + \text{H.c.}].\tag{2}$$

Here, there are two sublattices A and B with intracell hopping $\eta_1 = \eta_0[1 - \lambda \cos(\phi)]$ and intercell hopping $\eta_2 = \eta_0[1 + \lambda \cos(\phi)]$. This looks like a well-known SSH model and shares the same topology [45]. The modulating phase ϕ alters the hopping strength, which causes the system to go from topologically nontrivial phase ($\eta_2 > \eta_1$) to topologically trivial phase ($\eta_2 < \eta_1$) phase, which can be distinguished by the topological invariant quantity, winding number.

B. Coupling to an external field

The energy eigenvalues and eigenstate are calculated by using the field-free Hamiltonian H_0. The laser pulse is polarized along the linear chain and the Hamiltonian becomes time dependent $H(t) = H_0 + H_I(t)$. The length-gauge interaction Hamiltonian [21] reads as

$$H_I(t) = \sum_{n=1}^{N} nE(t)a_0 c_n c_n^\dagger, \quad (3)$$

where $a_0 = 2$ a.u. is the lattice constant, $E(t) = -dA(t)/dt$ is the electric field of the laser pulse, and the vector potential is $A(t) = A_0 \sin^2(\pi t/T)\sin(\omega_0 t)$. In this work, the amplitude of vector potential is kept as $A_0 = 0.1$ a.u., and the frequency of the laser is taken to be $\omega_0 = 0.0152$ a.u. ($\lambda = 3$ μm) for five optical cycles ($T = 5\tau$), where τ is one optical cycle of the fundamental frequency (ω_0).

The time-dependent Schrödinger equation is solved independently for the m initially occupied eigenstates $\psi_m(t = t_i)$ of the field-free Hamiltonian by the Crank-Nicolson method to get the time-dependent wave function $\psi_m(t)$. Total current is thus obtained as

$$J_{\text{total}}(t) = \sum_m \langle \psi_m(t)|J|\psi_m(t)\rangle, \quad (4)$$

where J current operator is defined as

$$J = -iea_0 \sum_n \eta[c_n^\dagger c_n - c_{n+1}^\dagger c_n]. \quad (5)$$

In order to extract the interband and intraband dynamics the time-dependent wave function $\psi_m(t)$ is projected to each field-free eigenstate [46]

$$|\psi(t)\rangle = \sum_b \sum_m \alpha_m^b(t)|\phi_m^b\rangle, \quad (6)$$

where b is the band index and m is the state index for every band. The intraband and interband current can be written as

$$J_{\text{intra}}^m(t) = \sum_b \sum_{m,m'} \alpha_m^{b*} \alpha_m^b \langle \phi_m^b|J|\phi_m^b\rangle, \quad (7)$$

$$J_{\text{inter}}^m(t) = \sum_{b,b'} \sum_{i,j} \alpha_i^{b*} \alpha_i^{b'} \langle \phi_i^b|J|\phi_i^{b'}\rangle. \quad (8)$$

The total current is the sum of intraband and interband current for each eigenstate m is calculated as

$$J_{\text{total}}(t) = \sum_m J_{\text{inter}}^m(t) + J_{\text{intra}}^m(t). \quad (9)$$

The harmonic spectra are obtained by taking the Fourier transform harmonics of the time derivative current, which are given as

$$S_{\text{total}}(\omega) = |\mathcal{F}_\omega[dJ_{\text{total}}/dt]|^2, \quad (10)$$

where $\mathcal{F}_\omega[g(t)] = \int g(t)\exp[-i\omega t]dt$ is the Fourier transform of the time-dependent function $g(t)$.

The total spectra [$S_{\text{total}}(\omega)$] of the emitted harmonics contain the summation of interband, intraband, and interference of both [16,47]

$$S_{\text{total}}(\omega) = S_{\text{inter}}(\omega) + S_{\text{intra}}(\omega) + S_{\text{intfer}}(\omega), \quad (11)$$
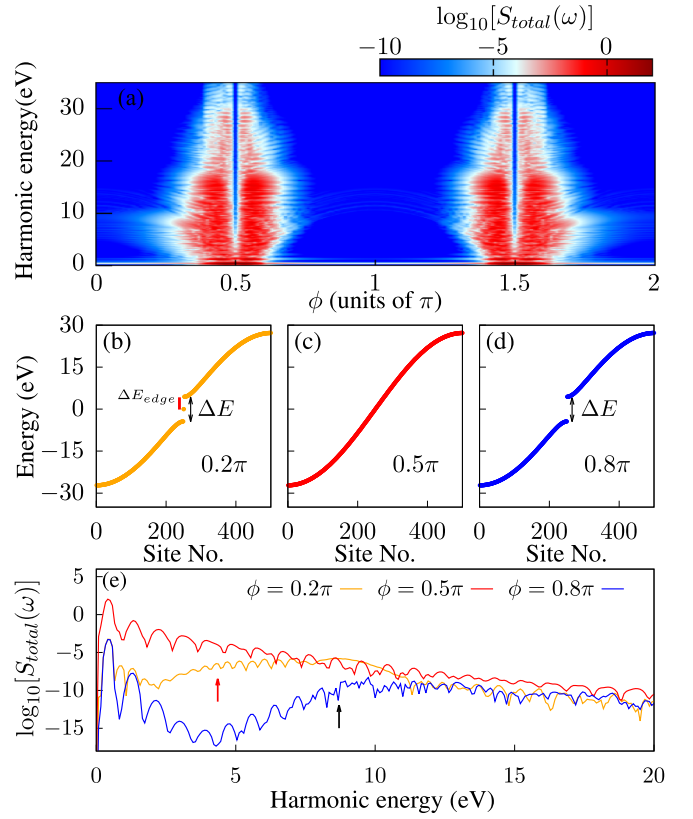

FIG. 2. The HHG spectrum is presented for each value of the modulating parameter (ϕ) in the Hamiltonian (H_0) [Eq. (10)]. The color bar represents the harmonic intensity. The energy spectrum for different topological phases, e.g., topologically nontrivial $\phi = 0.2\pi$ (b), gapless state $\phi = 0.5\pi$ (c), and trivial phase $\phi = 0.8\pi$ (d) are also compared. The harmonic spectra for these three ϕ values are also presented in (e). The black arrow in (b) and (d) represents ΔE, which is the energy difference between the last VB and CB, and the red line in (b) indicates ΔE_{edge}, which is the energy difference between the VB and the first edge state. The red arrow in (e) indicates ΔE_{edge} and the black arrow represents ΔE for both $\phi = 0.2\pi$ and $\phi = 0.8\pi$, which has similar ΔE.

where

$$S_{\text{inter,intra}}(\omega) = |\mathcal{F}_\omega[j_{\text{inter,intra}}]|^2 \quad (12)$$

and

$$S_{\text{intfer}}(\omega) = \mathcal{F}_\omega^*[j_{\text{inter}}]\mathcal{F}_\omega[j_{\text{intra}}] + \mathcal{F}_\omega^*[j_{\text{intra}}]\mathcal{F}_\omega[j_{\text{inter}}]. \quad (13)$$

The harmonic yield Y is calculated using the relation $Y = T^{-1}\int_{\omega_1}^{\omega_2} S_{\text{total}}(\omega)d\omega$.

III. RESULTS AND DISCUSSION

A. Chiral preserving system

The HHG spectrum calculated for all ϕ is shown in Fig. 2(a). We observed harmonic enhancements in the regions $\phi \in [0.3\pi, 0.6\pi]$ and $\phi \in [1.4\pi, 1.7\pi]$. In order to further examine this enhancement, three specific ϕ values are chosen: (i) $\phi = 0.2\pi$, Fig. 2(b) has a gapped state with the presence of edge state ($\eta_2 > \eta_1$); (ii) $\phi = 0.5\pi$, gapless state ($\eta_2 = \eta_1$)

in Fig. 2(c); and (iii) $\phi = 0.8\pi$, Fig. 2(d) has a gapped state with no edge state ($\eta_2 < \eta_1$).

Depending on the band gap (for each value of ϕ), the harmonic spectra show unique behavior. At $\phi = 0.2\pi$ and $\phi = 0.8\pi$, we can see a similar band gap (ΔE), which is marked (black arrow) in the energy spectrum [Figs. 2(b) and 2(d)] as well as a harmonic spectrum [Fig. 2(e)]. Intraband dynamics are dominant in the below band gap. The harmonic spectrum has a dip at $\phi = 0.8\pi$ [Fig. 2(e)], contributing to destructive interference among multiple valence electrons driven by the laser field [18]. However, at $\phi = 0.2\pi$, the harmonic yield increases after 4.3 eV, as marked by the red arrow in Fig. 2(e), which implies the zero-energy states facilitate the interband transitions. On the other hand, $\phi = 0.8\pi$ is a topologically trivial case with no midenergy states (edge states) and, thus, interband transitions occur after the electron surpasses the band gap (ΔE). As a consequence, there is a huge difference in the harmonic intensity. At $\phi = 0.5\pi$, the energy spectrum is gapless [Fig. 2(c)], and hence the contributions of both the bulk and edge states [Fig. 1(d)] result in an efficient harmonic intensity than the other two ϕ values. The reason for the harmonic intensity decreases after 3 eV will be discussed in detail in the upcoming section. The above variation in the harmonic emission allows us to distinguish between the topologically trivial and nontrivial phases in the harmonic spectrum, as was observed in previous studies of the HHG in chains.

The harmonic intensity is enhanced or decreased at certain ϕ values [Fig. 2(a)]; this can be understood by studying the energy bands. If the band gap is large (small), it is less (more) probable for an electron to excite to a conduction band, resulting in a lower- (higher-) harmonic yield observed in the region $\phi \in [0.6\pi, 0.8\pi]$ ($\phi \in [0.4\pi, 0.6\pi]$), where midenergy is enabling the transition to give a higher-harmonic yield in the region of $\phi \in [0, 0.4\pi]$ and the absence of midenergy state leads to a lower-harmonic yield in $\phi \in [0.6\pi, 1.3\pi]$. This behavior confirms the importance of the presence of an edge state, i.e., the nontrivial behavior of the system.

We have presented the band structure and harmonic spectrum around the range $\phi \in [0.4\pi, 0.6\pi]$ in Figs. 3(a) and 3(b) to analyze the nature of the HHG spectrum around the topological phase transitions. In this region, the energy difference between the bands is nearly zero, as also illustrated in Fig. 3(c), where the variation of ΔE and ΔE_{edge} with ϕ is presented. A similar harmonic yield [Fig. 3(b)] is observed below 2 eV in the range $\phi \in [0.44\pi, 0.49\pi]$ and $\phi \in [0.51\pi, 0.56\pi]$ with a sudden drop in the harmonic intensity at the topological phase transition ($\phi = 0.5\pi$) is observed. We did not see much harmonic enhancement in the topological phase compared to the trivial phase in this region. To emphasize this, we have taken the pair of ϕ values from the topological and trivial phases with similar band-gap energies. The HHG spectrum for $\phi = 0.4\pi$ and 0.6π is presented in Fig. 3(d). We observed the harmonic enhancement until 2 eV (below band gap) for $\phi = 0.4\pi$ as compared to $\phi = 0.6\pi$, indicating that the edge state facilitates transitions to the higher band in $\phi = 0.4\pi$. Similarly, in Fig. 3(e), a similar HHG spectrum is observed for $\phi = 0.44\pi$ and 0.56π (beyond the phase transition point value) because of the small band gap, not much contribution from edge states in $\phi = 0.44\pi$ is observed. However, for $\phi \in [0.4\pi, 0.49\pi]$, though it looks like a zero-energy state,
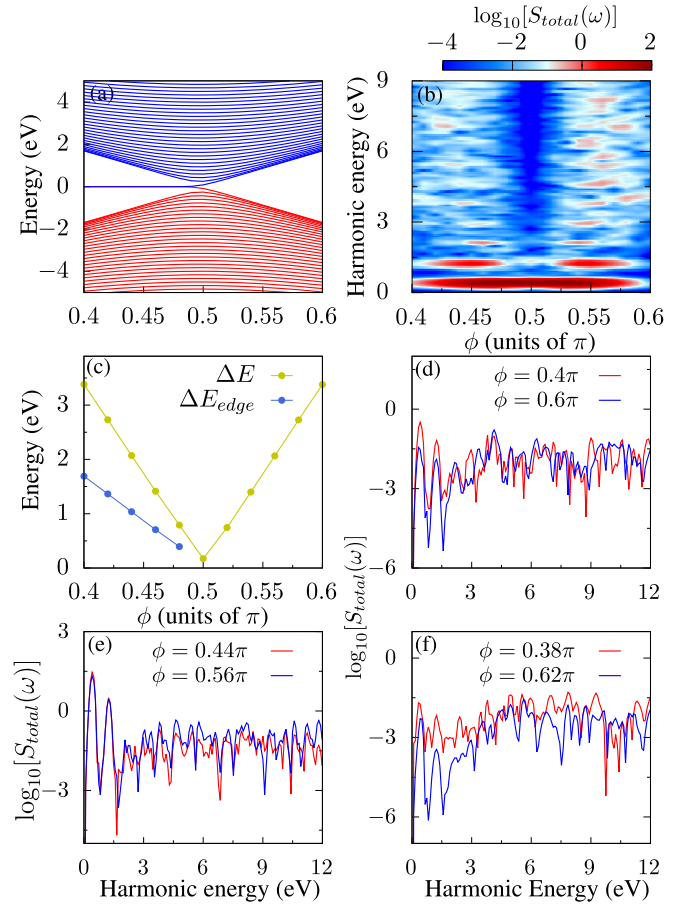

FIG. 3. (a) An expanded view of the energy spectrum around topological phase transitions in the region $\phi \in [0.4\pi, 0.6\pi]$, accompanied by the corresponding harmonic spectrum (b). In (c), we plot ΔE and ΔE_{edge} with respect to ϕ. The phase ϕ (which has the same band gap) are 0.4π and 0.6π in (d), 0.44π and 0.56π in (e), and 0.38π and 0.62π in (f).

the zoomed plot in Fig. 3(a) reveals exponential decay of the edge state to the bulk implying delocalization. We have already discussed that the change in the modulating parameter (ϕ) alters the localization strength [Figs. 1(b)–1(d)], which exhibits no role of the edge state in this region. On the trivial side ($\phi \in [0.51\pi, 0.6\pi]$), a small band gap enhances the transitions between the bands, leading to a similar HHG spectrum as the topological phase. Finally, the harmonic enhancement is visible in the topological case ($\phi = 0.38\pi$) as compared to the trivial case ($\phi = 0.62\pi$) as shown in Fig. 3(f), where the contribution from the edge states (~ 1.8 eV) can distinguish between the phases when the band gap is quite large.

To further elucidate this aspect of sudden drop in the harmonic emission at topological phase transitions, in Figs. 4(a)–4(c), we have presented the HHG spectra with interband and intraband harmonics when $\phi \in [0.49\pi, 0.51\pi]$. At $\phi = 0.49\pi$ [Fig. 4(a)], the intraband harmonics are comparable to the interband ones, and the interference effects have an impact only after the cutoff of ~ 35 eV. The HHG spectrum involving only the interference term is presented in Figs. 4(d)–4(f) [Eq. (13)]. The interference term has two contributions: the negative and positive values refer to destructive
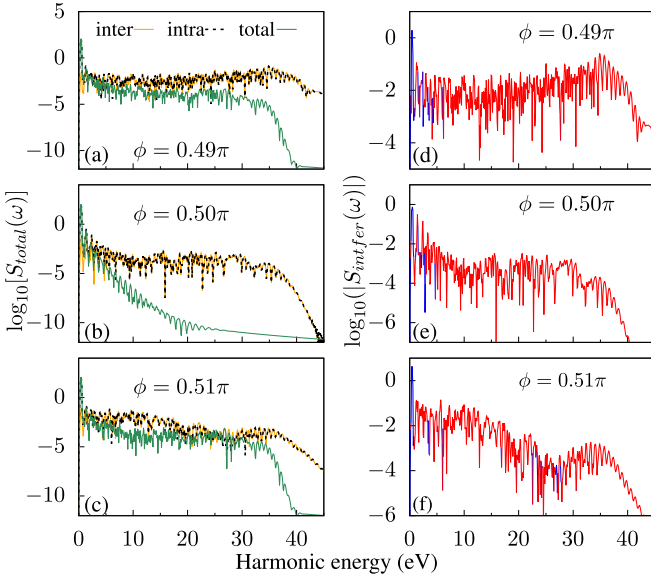
FIG. 4. HHG spectrum of total (black), intraband (green), and interband (red) are shown for $\phi = 0.49\pi$ (a), $\phi = 0.50\pi$ (b), and $\phi = 0.51\pi$ (c). The corresponding interference term $S_{\text{intfer}}(\omega)$ [Eq. (13)] in the logarithmic scale are presented for $\phi = 0.49\pi$ (d), $\phi = 0.50\pi$ (e), and $\phi = 0.51\pi$ (f).

and constructive interference causing the suppression or the enhancement of total harmonic yield, respectively. The negative values in the interference term cannot be plotted on a logarithmic scale, and hence, we have plotted the absolute value in Figs. 4(d)–4(f). The different colors in the spectrum distinguish between a negative (red) and a positive (blue) contribution.

It can be observed that the strong destructive interference happens at a cutoff for $\phi = 0.49\pi$ [Fig. 4(d)], which correspondingly reduces the total harmonic yield. In Fig. 4(e), for $\phi = 0.5\pi$ the interference term significantly suppresses total HHG spectrum. The deviation from intraband and interband contributions in Fig. 4(b) clearly indicates the strong presence of the destructive interference. The suppression of the total harmonic spectrum can also be seen in the ϕ-dependent plot [refer to Fig. 3(b)]. The total harmonic spectrum intensity decrease around 10 eV at $\phi = 0.51\pi$ [Fig. 4(c)], which correlates with the dominant destructive interference term in Fig. 4(f). In all the above cases, where the band gap is small, the intraband and interband current oscillations occur simultaneously when the interband current rises and the intraband falls, and vice versa. This helps us to conclude that both current oscillations are out of phase with each other in the time domain and have a similar intensity in the Fourier domain [16].

B. System with broken chiral symmetry

In this section, we study how the breaking of the chiral symmetry affects the HHG spectrum. Chiral symmetry can be broken either by introducing the onsite potential [19], or next-nearest-neighbor hopping potential [44,48], which have been experimentally demonstrated in photonic crystals [49]. Here, we specifically see the inclusion of the onsite potential terms
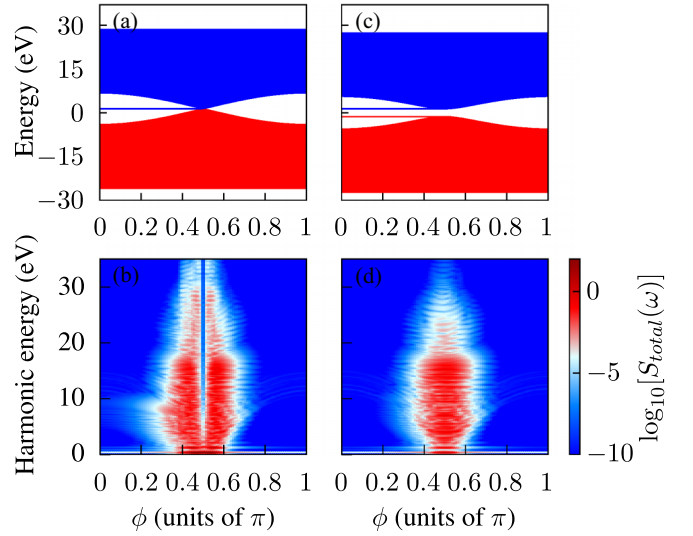

FIG. 5. The energy spectrum for different values of ϕ is presented for the case when the onsite potential $V_A = V_B = 0.05$ a.u. (a) and $V = 0.05 \cos(2\pi bn)$ a.u. (b). The respective HHG spectra as a function of ϕ is illustrated in (c) and (d), respectively.

as $H_\mu = \sum_{n=1}^{N} [V_A c_{n,A}^\dagger c_{n,A} + V_B c_{n,B}^\dagger c_{n,B}] + H_0$, where V_A and V_B are the strengths of the onsite potential. We first consider the case with $V_A = V_B = 0.05$.

Figure 5(a) shows the energy spectrum, which is similar to Fig. 1(a). However, the degenerate edge states are shifted by 1.3 eV (0.05 a.u.) from the zero scales. This shift in the energy of the edge state is caused by the presence of the onsite potential, which will not change the physical aspects of the HHG spectra. As a result, a similar [Fig. 2(a)] harmonic spectrum is observed in Fig. 5(b) as well. The energy and HHG spectra have a mirror symmetry with respect to $\phi = 1\pi$. So hereafter, we present the plot up to $\phi = 1\pi$. Next, we consider the onsite potential, with a cosine modulation $V = 0.05 \cos(2\pi bn)$ leads to $V = 0.05(-1)^n$. Hence, depending on the site number (n), the different onsite strengths for two sublattices (A and B) are $V_A = -V_B = -0.05$. The energy spectrum with this cosine modulation is shown in Fig. 5(c). In this case of cosine modulation, the energy spectrum split into two bands with increased band gap. This leads to the edge states being split into two branches away from zero. As we continuously sweep the parameter ϕ, the edge states mix with the bulk around $\phi = 0.5\pi$. As a result, different behaviors in the HHG spectra are observed [Fig. 5(d)]. In the chiral breaking case, the harmonic emission intensity enhanced around $\phi \in [0.4\pi, 0.6\pi]$ as can be seen from Fig. 5(d), and there is no reduction of the harmonic yield for $\phi = 0.5\pi$, as was the case with Fig. 2(b). The larger band gap for chiral breaking case [Fig. 5(d)] lowers the contribution from the interference of interband and intraband harmonics, and hence the total harmonic yield is not reduced. In contrast, the band gap is near zero in the chiral preserving system around the topological phase transition [refer to Fig. 3], and the interband and intraband oscillations are comparable (refer to Fig. 4). Hence, the interference term has a crucial impact on reducing the total harmonic spectrum [Fig. 2(b)], especially in $\phi = 0.5\pi$ the total harmonic spectrum is severely suppressed.
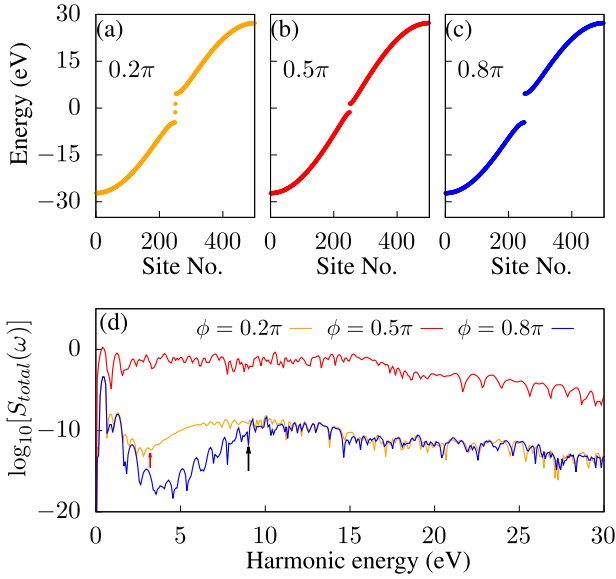
FIG. 6. The energy spectrum for the case with $V_A = -V_B$ is presented for three different ϕ values: (a) $\phi = 0.2\pi$, (b) $\phi = 0.5\pi$, and (c) $\phi = 0.8\pi$, along with the harmonic emission spectra (d). In (d), for $\phi = 0.2\pi$ case the red arrow around ~ 3.2 eV represents the ΔE_{edge}, however, the black arrow around ~ 9 eV represented the ΔE for $\phi = 0.2\pi$ and 0.8π cases.

We have considered three different ϕ values, namely, $\phi = 0.2\pi$, 0.5π, and 0.8π to explore the the harmonic emission weakens for $V_A = -V_B$ [Fig. 5(d)] as compared to the chiral preserving system [Fig. 2(a)]. The corresponding band structure and harmonic spectrum for these selected ϕ values are illustrated in Figs. 6(a)–6(d). We can see that harmonic intensity increases around ~ 3.2 eV for $\phi = 0.2\pi$, as marked in the red arrow in Fig. 6(d), which corresponds to a transition between the valence band and the lower edge state (ΔE_{edge}). Interband transitions happen directly to the conduction band from the lower edge state because they inhibit the transitions between the two edge states, which are localized at the opposite boundaries of the chains. This reflects the lower harmonic yield in the below band-gap region at $\phi = 0.2\pi$ compared to chiral preserving systems [refer to Fig. 2(d)]. The harmonic intensity at $\phi = 0.8\pi$ is less than $\phi = 0.2\pi$, confirming the edge state's absence. The black arrow in Fig. 6(d) represents the minimum band gap for $\phi = 0.2\pi$ and 0.8π. The band structure for $\phi = 0.5\pi$ is gapped [Fig. 6(c)], and the higher-harmonic emission was observed [Fig. 6(d)] for this case because of the small band gap compared to other ϕ values.

C. HHG yield

The effect of the control parameter ϕ on the harmonic yield in the energy range 3–9 eV is studied and presented in Fig. 7. The energy differences ΔE and ΔE_{edge} as a function of the parameter ϕ are illustrated in Figs. 7(a) and 7(b), respectively, for off-diagonal hopping and $V_A = -V_B$ onsite potential model. As ϕ changes, the intercell hopping strength (η_2) weakens [Eq. (2)], and the band gap reduces until $\phi = 0.5\pi$ as shown in Fig. 7(a). After topological transitions, the intracell hopping strength (η_1) increases with ϕ, which opens a band
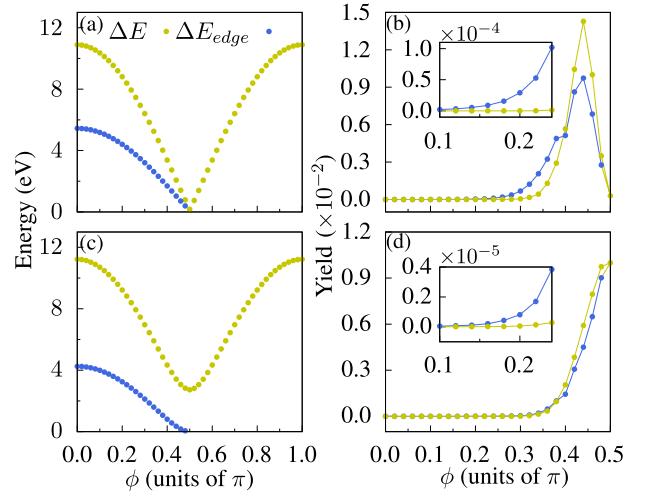

FIG. 7. ΔE and ΔE_{edge} are plotted with ϕ for the cases without (off-diagonal hopping model) (a) and with (c) onsite potential, and respective harmonic yield in the 3–9 eV energy range is presented as a function of the modulating phase (ϕ) for the off-diagonal hopping model (b), and onsite potential ($V_A = -V_B$) (d). The mirror symmetry of energy spectrum around $\phi = 0.5\pi$ enabled us to map the harmonic yield for the cases with $\phi \in [0.5\pi, 1\pi]$ on $\phi \in [0, 0.5\pi]$. This helps us to clearly see the role of the edge states in the harmonic yield. In (b) and (d), the blue line points represent the case for $\phi \in [0, 0.5\pi]$, which is topological nontrivial and having the edge states. However, yellow line points are for the case when $\phi \in [0.5\pi, 1\pi]$ showing trivial phase. The inset plot represents the harmonic yield zoomed in the range $\phi \in [0, 0.24\pi]$.

gap [Fig. 7(a)]. Figure 7(a) shows that the ΔE has a mirror symmetry with respect to $\phi = 0.5\pi$. So in Fig. 7(b), we have folded back the harmonic yield values for the trivial phase (after $\phi = 0.5\pi$) and plotted into the $\phi = 0.5\pi$. The different colors can differentiate between the topological phase (blue) and the trivial phase (yellow). The appreciable harmonic yield starts at $\phi = 0.25\pi$, which has the midenergy state to enhance the transitions until $\phi = 0.44\pi$ and then harmonic yield starts decreases until the topological phase transitions happen at $\phi = 0.5\pi$. After topological phase transitions, harmonic yield increases until $\phi = 0.56\pi$ beyond that; the harmonic yield rapidly decreases because the absence of midenergy dictates the lower-harmonic yield.

To emphasize the fact that there is less harmonic yield after $\phi = 0.44\pi$ and an enhanced yield for $\phi \in [0.52\pi, 0.58\pi]$ as compared to this $\phi \in [0.42\pi, 0.48\pi]$ [Fig. 7(b)]. We have taken the two ϕ values, at $\phi = 0.44\pi$ and 0.56π, which represent the highest yield, and the corresponding interference term is presented in Figs. 8(a) and 8(b). The interference spectrum oscillates between constructive (blue) and destructive interference (red). The black dotted line in Figs. 8(a) and 8(b) shows that after ~ 6 eV, destructive interference strength for $\phi = 0.56\pi$ starts decreasing compared to $\phi = 0.44\pi$, which implies a higher yield at $\phi = 0.56\pi$. The interference terms for $\phi = 0.48\pi$ and 0.52π are plotted in Figs. 8(c) and 8(d). The strong destructive interference in both the ϕ values reduces the total spectra, resulting in a lower-harmonic yield. On the topological side, the edge states are not enhancing the transitions from VB to CB after $\phi = 0.4\pi$ (refer to Fig. 3). We
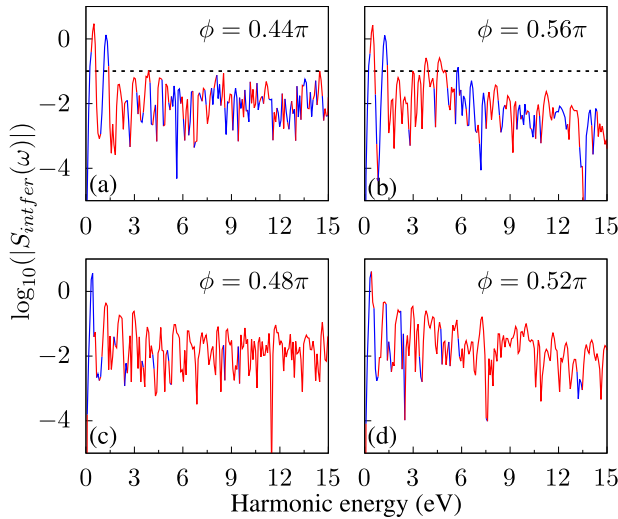
FIG. 8. Comparing the inteference term of $S_{\text{intfer}}(\omega)$ [Eq. (13)] between the topologically nontrivial (left column, $\phi < 0.5\pi$) and trivial (right column, $\phi > 0.5\pi$) phase values. The red and blue colors indicate destructive and constructive interference, respectively.

have already seen that in this region, the edge state approaches the bands, so there is a mixing of transition popups between the intraband and interband. We cannot say which dominates in this scenario because both transitions happen simultaneously, as shown in Figs. 4(a)–4(c). Therefore, the interference term dominates this region, and the trivial side absence of an edge state leads to fewer interference effects that enhance the harmonic yield for $\phi \in [0.52\pi, 0.58\pi]$, compared to $\phi \in [0.42\pi, 0.48\pi]$ [Fig. 7(b)]. Moreover, when there is a smaller band gap, the interference effects play a dominant role in reducing the harmonic yield. The zoomed inset plot around $\phi \in [0.1\pi, 0.24\pi]$ still shows the enhanced yield in the topological phase. The harmonic yield is a robust measure that distinguishes emission spectra between the topologically trivial and nontrivial phases.

Similarly, the harmonic yield is calculated by adding an onsite potential. The harmonic yield for the $V_A = V_B$ case is not shown; it has just the shifted energy spectrum, and the yield is the same as in Fig. 7(b). The different onsite strength inside the sublattice with $V_A = -V_B$ opens a gap in the energy spectrum [Fig. 7(c)], which lifts the degenerate edge states. This implies that the edge states are not precisely located at half of the band gap, whereas in off-diagonal case both the edge states are located at zero. The electron transition probability is less because the large band gap between the first edge state and the VB leads to a lower efficiency for $\phi \leqslant 0.38\pi$, as presented in Fig. 7(d). The efficiency found to be enhanced for $\phi \in [0.4\pi, 0.6\pi]$, which implicitly relates to the minimum band gap. In this range, a larger band gap [Fig. 7(c)] than the off-diagonal case [Fig. 7(a)], interband transition is dominant compared to intraband transitions, indicating less interference effects. Hence, we observed a similar harmonic yield for $\phi \in [0.4\pi, 0.49\pi]$ and $\phi \in [0.51\pi, 0.60\pi]$. The zoomed-inset plot [Fig. 7(d)] reveals an enhanced yield in the topological phase. The position of the edge state plays a crucial role in strengthening the harmonic emission. Breaking the chiral symmetry reduces the window of harmonic emissions.
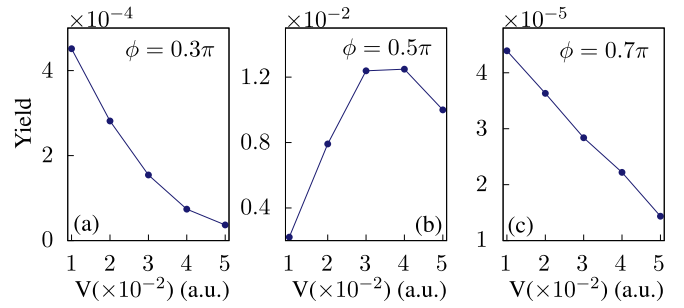

FIG. 9. The harmonic yield is calculated with the variation of the onsite potential ($V_A = -V_B$) strength for different ϕ values. The scaling factors are specified in each plot.

So far, we have learned that the efficiency of the harmonic yield is a good measure for identifying the topological phases. The increase or decrease of the harmonic yield is related to the minimum or maximum band gap along with the presence of the edge states. To elucidate the lower-harmonic yield obtained in the $V_A = -V_B$ case [Fig. 7(d)], we have also studied the harmonic yield with the variation of the onsite strength ranging from $V = 0.01$–0.05 a.u. The variation of the harmonic yield with the strength of the onsite potential is presented in Fig. 9 for different values of ϕ. It can be seen from Fig. 9 that for the case of $\phi = 0.3\pi$ and 0.7π, the harmonic yield decreases with the increase in onsite potential strength. However, for $\phi = 0.5\pi$ case the reverse happens. The results of Figs. 9(a) and 9(c) can be understood from the fact that the band gap between VB and CB increases with potential strength. Moreover, for $\phi = 0.5\pi$ case [Fig. 9(b)] too the band gap increases with the onsite potential strength, however, the reduction in the contribution from the interference term enhances the total harmonic yield.

In order to examine the harmonic yield enhancement for $\phi = 0.5\pi$, we have presented the band-gap energy ΔE for $\phi = 0.5\pi$ with different onsite potential strength [Fig. 10(a)]. It clearly shows that the band gap varies significantly against onsite strengths. The respective HHG spectra for the case of $\phi = 0.5\pi$ for different onsite potentials are also presented [Fig. 10(b)]. We have already seen that the lower band gap leads to destructive interference, reducing the total HHG
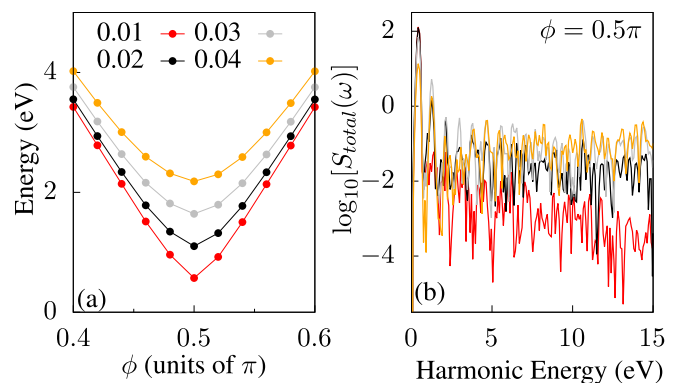

FIG. 10. The band-gap energy ΔE for $\phi = 0.5\pi$ is presented when the onsite potential is $V_A = -V_B$ (a) with different onsite strengths, and the corresponding HHG spectrum is plotted in (b).

spectra. This explains the increase of higher-harmonic yield with onsite potential strength $\phi = 0.5\pi$. The above analysis shows that for $\phi = 0.5\pi$, there is an interesting feature in the variation of onsite strength. Hence, the harmonic yield detects crucial aspects of the AAH model.

IV. SUMMARY

In summary, we have investigated the high-harmonic generation in the different topological phases of off-diagonal hopping in the AAH model with a commensurate modulation, which gives rise to a zero-energy edge state by keeping the chiral symmetry intact. The modulating phase (ϕ) of the AAH model is used as a control parameter which causes the system to go from a topologically nontrivial phase to a topologically trivial phase. The HHG yield shows a strong dependence on the control parameter and enables us to make the distinction between the different phases. The edge states of the topological nontrivial phase assist in the enhancement of the harmonic yield. In contrast, the absence of edge states leads to a lower-harmonic yield. The harmonic yield is found to be minimal when the control parameter is around the phase transition point, i.e., $\phi = 0.5\pi$. The interference of the interband and intraband harmonics dominates the outcome of the harmonic yield near the topological phase transition (band gap is near zero). Furthermore, the impact of chiral symmetry breaking in the HHG spectrum is also explored by adding an onsite potential in two different ways: $V = V_A = V_B$ and $-V = V_A = -V_B$, and the offset of the edge states found to play a crucial role in harmonic enhancement. Our work presents the HHG yield as a robust measure to detect topological phase transitions. It is also observed that the onsite strength can control the harmonic emission of the systems with broken chiral symmetry. Explicit dependence of HHG processes on higher dimensions and the decoherence we reserve for the future.

[1] F. Krausz and M. Ivanov, Attosecond physics, Rev. Mod. Phys. **81**, 163 (2009).

[2] O. Smirnova, Y. Mairesse, S. Patchkovskii, N. Dudovich, D. Villeneuve, P. Corkum, and M. Y. Ivanov, High harmonic interferometry of multi-electron dynamics in molecules, Nature (London) **460**, 972 (2009).

[3] P. B. Corkum and F. Krausz, Attosecond science, Nat. Phys. **3**, 381 (2007).

[4] S. Ghimire, A. D. DiChiara, E. Sistrunk, P. Agostini, L. F. DiMauro, and D. A. Reis, Observation of high-order harmonic generation in a bulk crystal, Nat. Phys. **7**, 138 (2011).

[5] T. T. Luu, M. Garg, S. Y. Kruchinin, A. Moulet, M. T. Hassan, and E. Goulielmakis, Extreme ultraviolet high-harmonic spectroscopy of solids, Nature (London) **521**, 498 (2015).

[6] S. Y. Kruchinin, F. Krausz, and V. S. Yakovlev, *Colloquium:* Strong-field phenomena in periodic systems, Rev. Mod. Phys. **90**, 021002 (2018).

[7] Z. Nourbakhsh, N. Tancogne-Dejean, H. Merdji, and A. Rubio, High harmonics and isolated attosecond pulses from MgO, Phys. Rev. Appl. **15**, 014013 (2021).

[8] G. Vampa, T. J. Hammond, N. Thiré, B. E. Schmidt, F. Légaré, C. R. McDonald, T. Brabec, D. D. Klug, and P. B. Corkum, All-optical reconstruction of crystal band structure, Phys. Rev. Lett. **115**, 193603 (2015).

[9] A. Pattanayak, Mrudul M. S., and G. Dixit, Influence of vacancy defects in solid high-order harmonic generation, Phys. Rev. A **101**, 013404 (2020).

[10] N. Yoshikawa, T. Tamaya, and K. Tanaka, High-harmonic generation in graphene enhanced by elliptically polarized light excitation, Science **356**, 736 (2017).

[11] M. S. Mrudul and G. Dixit, High-harmonic generation from monolayer and bilayer graphene, Phys. Rev. B **103**, 094308 (2021).

[12] N. Yoshikawa, K. Nagai, K. Uchida, Y. Takaguchi, S. Sasaki, Y. Miyata, and K. Tanaka, Interband resonant high-harmonic generation by valley polarized electron–hole pairs, Nat. Commun. **10**, 3709 (2019).

[13] O. Schubert, M. Hohenleutner, F. Langer, B. Urbanek, C. Lange, U. Huttner, D. Golde, T. Meier, M. Kira, S. W. Koch, and R. Huber, Sub-cycle control of terahertz high-harmonic generation by dynamical bloch oscillations, Nat. Photon. **8**, 119 (2014).

[14] Nivash R, A. R. Holkundkar, and J. N. Bandyopadhyay, Temporal control of high-order harmonic cutoffs in periodic crystals, Phys. Rev. A **108**, 063503 (2023).

[15] D. J. Thouless, M. Kohmoto, M. P. Nightingale, and M. den Nijs, Quantized Hall conductance in a two-dimensional periodic potential, Phys. Rev. Lett. **49**, 405 (1982).

[16] A. R. Holkundkar, Nivash R, and J. N. Bandyopadhyay, Role of interband and intraband current in laser interaction with bichromatic quasiperiodic crystals, Phys. Rev. B **109**, 155155 (2024).

[17] D. Bauer and K. K. Hansen, High-harmonic generation in solids with and without topological edge states, Phys. Rev. Lett. **120**, 177401 (2018).

[18] H. Jürß and D. Bauer, High-harmonic generation in Su-Schrieffer-Heeger chains, Phys. Rev. B **99**, 195428 (2019).

[19] C. Ma, X.-B. Bian, and T.-Y. Du, Role of symmetry breaking in high-order harmonic generation from Su-Schrieffer-Heeger systems, Phys. Rev. B **106**, 125117 (2022).

[20] M. L. Bera, J. O. de Almeida, M. Dziurawiec, M. Płodzień, M. M. Maśka, M. Lewenstein, T. Grass, and U. Bhattacharya, Topological phase detection through high-harmonic spectroscopy in extended Su-Schrieffer-Heeger chains, Phys. Rev. B **108**, 214104 (2023).

[21] J.-Q. Liu and X.-B. Bian, Detection of edge states by high-order harmonic generation in the Harper model, Phys. Rev. B **105**, 054308 (2022).

[22] A. Pattanayak, S. Pujari, and G. Dixit, Role of Majorana fermions in high-harmonic generation from Kitaev chain, Sci. Rep. **12**, 6722 (2022).

[23] N. Baldelli, U. Bhattacharya, D. González-Cuadra, M. Lewenstein, and T. Graß, Detecting Majorana zero modes via strong field dynamics, ACS Omega **7**, 47424 (2022).

[24] R. E. F. Silva, Á. Jiménez-Galán, B. Amorim, O. Smirnova, and M. Ivanov, Topological strong-field physics on sub-laser-cycle timescale, Nat. Photon. **13**, 849 (2019).

[25] C. Heide, Y. Kobayashi, D. R. Baykusheva, D. Jain, J. A. Sobota, M. Hashimoto, P. S. Kirchmann, S. Oh, T. F. Heinz, D. A. Reis, and S. Ghimire, Probing topological phase transitions using high-harmonic generation, Nat. Photon. **16**, 620 (2022).

[26] A. Chacón, D. Kim, W. Zhu, S. P. Kelly, A. Dauphin, E. Pisanty, A. S. Maxwell, A. Picón, M. F. Ciappina, D. E. Kim, C. Ticknor, A. Saxena, and M. Lewenstein, Circular dichroism in higher-order harmonic generation: Heralding topological phases and transitions in Chern insulators, Phys. Rev. B **102**, 134115 (2020).

[27] O. Neufeld, N. Tancogne-Dejean, H. Hübener, U. De Giovannini, and A. Rubio, Are there universal signatures of topological phases in high-harmonic generation? Probably not., Phys. Rev. X **13**, 031011 (2023).

[28] Y. Lahini, R. Pugatch, F. Pozzi, M. Sorel, R. Morandotti, N. Davidson, and Y. Silberberg, Observation of a localization transition in quasiperiodic photonic lattices, Phys. Rev. Lett. **103**, 013901 (2009).

[29] M. Verbin, O. Zilberberg, Y. Lahini, Y. E. Kraus, and Y. Silberberg, Topological pumping over a photonic Fibonacci quasicrystal, Phys. Rev. B **91**, 064201 (2015).

[30] M. Verbin, O. Zilberberg, Y. E. Kraus, Y. Lahini, and Y. Silberberg, Observation of topological phase transitions in photonic quasicrystals, Phys. Rev. Lett. **110**, 076403 (2013).

[31] Y. E. Kraus and O. Zilberberg, Topological equivalence between the Fibonacci quasicrystal and the Harper model, Phys. Rev. Lett. **109**, 116404 (2012).

[32] F. Liu, S. Ghosh, and Y. D. Chong, Localization and adiabatic pumping in a generalized Aubry-André-Harper model, Phys. Rev. B **91**, 014108 (2015).

[33] S. Ganeshan, K. Sun, and S. Das Sarma, Topological zero-energy modes in gapless commensurate Aubry-André-Harper models, Phys. Rev. Lett. **110**, 180403 (2013).

[34] J. C. C. Cestari, A. Foerster, and M. A. Gusmão, Fate of topological states in incommensurate generalized Aubry-André models, Phys. Rev. B **93**, 205441 (2016).

[35] L.-J. Lang, X. Cai, and S. Chen, Edge states and topological phases in one-dimensional optical superlattices, Phys. Rev. Lett. **108**, 220401 (2012).

[36] S. Ryu, A. P. Schnyder, A. Furusaki, and A. W. W. Ludwig, Topological insulators and superconductors: tenfold way and dimensional hierarchy, New J. Phys. **12**, 065010 (2010).

[37] C.-K. Chiu, J. C. Y. Teo, A. P. Schnyder, and S. Ryu, Classification of topological quantum matter with symmetries, Rev. Mod. Phys. **88**, 035005 (2016).

[38] Y.-Y. Lv, J. Xu, S. Han, C. Zhang, Y. Han, J. Zhou, S.-H. Yao, X.-P. Liu, M.-H. Lu, H. Weng, Z. Xie, Y. B. Chen, J. Hu, Y.-F. Chen, and S. Zhu, High-harmonic generation in Weyl semimetal β-WP$_2$ crystals, Nat. Commun. **12**, 6437 (2021).

[39] A. Bharti, M. Ivanov, and G. Dixit, How massless are Weyl fermions in Weyl semimetals, Phys. Rev. B **108**, L020305 (2023).

[40] Z.-Y. Chen and R. Qin, Probing structural chirality of crystals using high-order harmonic generation in solids, Phys. Rev. A **101**, 053423 (2020).

[41] T. Heinrich, M. Taucer, O. Kfir, P. B. Corkum, A. Staudte, C. Ropers, and M. Sivis, Chiral high-harmonic generation and spectroscopy on solid surfaces using polarization-tailored strong fields, Nat. Commun. **12**, 3723 (2021).

[42] Y. E. Kraus, Y. Lahini, Z. Ringel, M. Verbin, and O. Zilberberg, Topological states and adiabatic pumping in quasicrystals, Phys. Rev. Lett. **109**, 106402 (2012).

[43] J. K. Asbóth, L. Oroszlány, and A. Pályi, *A Short Course on Topological Insulators* (Springer, Cham, 2016).

[44] J. Cao, Y. Xing, L. Qi, D.-Y. Wang, C.-H. Bai, A.-D. Zhu, S. Zhang, and H.-F. Wang, Simulating and studying the topological properties of generalized commensurate Aubry–André–Harper model with microresonator array, Laser Phys. Lett. **15**, 015211 (2018).

[45] W. P. Su, J. R. Schrieffer, and A. J. Heeger, Solitons in polyacetylene, Phys. Rev. Lett. **42**, 1698 (1979).

[46] X. Liu, X. Zhu, X. Zhang, D. Wang, P. Lan, and P. Lu, Wavelength scaling of the cutoff energy in the solid high harmonic generation, Opt. Express **25**, 29216 (2017).

[47] X.-Q. Wang, Y. Xu, X.-H. Huang, and X.-B. Bian, Interference between inter- and intraband currents in high-order harmonic generation in solids, Phys. Rev. A **98**, 023427 (2018).

[48] L. Li, Z. Xu, and S. Chen, Topological phases of generalized Su-Schrieffer-Heeger models, Phys. Rev. B **89**, 085111 (2014).

[49] Z.-Q. Jiao, S. Longhi, X.-W. Wang, J. Gao, W.-H. Zhou, Y. Wang, Y.-X. Fu, L. Wang, R.-J. Ren, L.-F. Qiao, and X.-M. Jin, Experimentally detecting quantized Zak phases without chiral symmetry in photonic lattices, Phys. Rev. Lett. **127**, 147401 (2021).